ADVANCED FUNCTIONAL MATERIALS
www.afm-journal.de

Microenvironment Modulation of Single Cobalt Sites in Covalent Organic Frameworks with Serrated Stacking of Metallocorroles for Boosting Electrocatalytic Water Oxidation

Xikai Chen, Jinyu Liu, Changgui Lv, Yu Yan, Hongpo Liu, Yun-Lei Peng, Yanming Zhao, Thamraa AlShahrani, Peter E. VanNatta, and Shengqian Ma**

The electrochemical oxygen evolution reaction (OER) is critically influenced by the rate-determining step (RDS) and intermediate binding at catalytic sites, yet achieving precise control over these factors to promote the OER remains challenging. Enzymatic systems exemplify how catalytic efficiency is dictated by not only active centers but also their surrounding microenvironments. Drawing inspiration from this paradigm, serrated stacking cobalt-corrole-based covalent organic frameworks (Co-CorCOFs) with well-defined active sites are developed as models for systematical investigation and manipulation of electrocatalytic behavior. It is shown that remote microenvironment tuning via oriented functionalization of COF linkages effectively alters the electronic structures of both the COF backbone and Co sites. This results in distinct reaction kinetics and electron transfer in covalently assembled composite Co-CorCOF/carbon nanotube (CNT) hybrids (Co-CorCOF@CNTs). Notably, introducing quinoline moieties into the linkages significantly boosts OER activity in Co-CorCOF-3@CNT versus an unmodified Co-CorCOF-2@CNT. Mechanistic studies reveal that microenvironment engineering fine-tunes the Co sites' d-band center, which facilitates oxygenated intermediate adsorption and shifts the RDS from *OH formation to *OH deprotonation with a substantial reduction in the energy barrier, thereby accelerating the reaction rate. This work offers a new avenue for the formulation of more efficient catalysts via a molecular-level microenvironment modulation strategy.

1. Introduction

The electrochemical oxygen evolution reaction (OER) plays a pivotal role in advanced energy conversion technologies, such as fuel cells, overall water-splitting systems, and metal–air batteries.[1,2] However, the OER is hindered by sluggish kinetics, primarily due to the complex extraction of four electrons from two water molecules, cleavage of strong O—H bonds, and formation of energetically demanding O—O bonds.[3–5] Consequently, the development of efficient water oxidation catalysts (WOCs) for enabling effective interconversion between electrical and chemical energy is a significant challenge. Molecular WOCs, particularly transition metal complexes, offer distinct advantages due to their well-defined and tunable structures, which can be systematically functionalized to attain high catalytic activity and facilitate detailed mechanistic studies.[6] Nevertheless, homogeneous catalysts face significant limitations, such as their reliance on organic media, susceptibility to deactivation, and inefficient electron transfer, which restrict their widespread application. To address

X. Chen, J. Liu, C. Lv, Y. Yan, H. Liu, Y. Zhao
Henan Institute of Advanced Technology
Zhengzhou University
Zhengzhou 450003, China
E-mail: yanmingzhao@zzu.edu.cn

Y.-L. Peng
College of Science
China University of Petroleum (Beijing)
Beijing 102249, China

T. AlShahrani
Department of Physics
College of Science
Princess Nourah bint Abdulrahman University
Riyadh 11564, Saudi Arabia

P. E. VanNatta, S. Ma
Department of Chemistry
University of North Texas
Denton, TX 76201, USA
E-mail: Shengqian.Ma@unt.edu

The ORCID identification number(s) for the author(s) of this article can be found under https://doi.org/10.1002/adfm.202511972

DOI: 10.1002/adfm.202511972

these challenges, the incorporation of well-characterized molecular WOCs within conductive substrates to create heterogeneous systems has emerged as a promising strategy, benefiting catalytic efficiency, ease of separation, reusability, and durability.[7–10]

In recent years, covalent organic frameworks (COFs) have received increasing attention as a novel class of porous materials characterized by their large surface area, high crystallinity, and exceptional structural diversity.[11–13] These properties, coupled with their remarkable compositional and structural designability, make COFs an appealing scaffold for the integration of functional molecular WOCs, thereby facilitating their heterogenization. We rationalize that COFs incorporating molecular WOCs as constitutional units hold immense potential as electrocatalytic materials for OER for several reasons. 1) The long-range order and porosity of COFs enable the creation of well-defined, highly dispersed active sites. 2) Their readily modifiable structures allow for tailored functionalization.[14,15] 3) Strong covalent bonds, particularly irreversible linkages, confer exceptional stability.[16] 4) Extensive π-conjugation systems can enhance conductivity. 5) Structural modulation strategies, such as regulating 2D COF stacking modes,[17,18] constructing 3D frameworks,[19] and exfoliating 2D COFs,[20] improve site accessibility and mass transport. Despite these advantages, research on COFs for electrocatalytic OER has predominantly focused on introducing electroactive metal complexes,[21–25] yielding encouraging but limited results.

In addition to the intrinsic properties of active metal sites, the surrounding physicochemical microenvironment can also play a crucial role in determining electrochemical activity, as demonstrated by natural enzyme catalysis and experimental studies.[26–31] Molecular catalyst incorporated COFs, with their atomically precise and customizable structures, as well as isolated and highly dispersed catalytic sites, offer an ideal platform for systematical manipulation of the active site microenvironment.[32,33] This not only offers an avenue to enhance electrocatalytic efficiency but also facilitates detailed mechanistic investigations and the establishment of reliable structure–activity relationships to guide subsequent improvement. Of specific note, microenvironment modulation poses the potential to influence the binding strength of intermediates, alter the rate-determining step (RDS), and modify the associated energy barriers, ultimately optimizing catalytic performance.[32–34] Inspired by these insights, it is highly desirable to construct suitable COF models to delve into the impact of the chemical microenvironment on catalytic behavior, which remains unexplored for electrochemical OER.

Corroles, a class of 18-π-conjugated macrocyclic compounds within the porphyrinoid family, have attracted significant interest due to their unique physicochemical properties.[35–39] Particularly, their trianionic nature enables the stabilization of high-valent metal ions, which are often implicated in the key O—O bond formation step, making metallocorroles highly promising for electrocatalytic water oxidation.[40–44] Nevertheless, to the best of our knowledge, no studies have reported the use of metallocorrole-based COFs for OER despite their potential for expanding structural and functional diversity and enhancing performance. Notably, although our research group successfully synthesized the first corrole-based COF (CorCOF-1) in 2020,[38] its nonuniform local environment, a consequence of the C_{2v}-symmetric tridentate corrole units, limits its utility for probing microenvironment–catalysis relationships. These considerations underscore the need for rationally designed metallocorrole-COFs to elucidate the mechanistic role of the chemical microenvironment in promoting electrocatalytic OER.

Herein we report the synthesis of a linear corrole monomer for constructing a novel imine-linked COF, designated as CorCOF-2. This framework features a high-symmetry *hcb* topology and a unique serrated stacking architecture, serving as an excellent model platform for exploring the application of metallocorrole-based COFs in electrochemical OER and elucidating microenvironment contributions (**Scheme 1**). Leveraging the strategy of COF linkage functionalization, two covalently hybrid materials (Co-CorCOF-2@CNT and Co-CorCOF-3@CNT) synthesized via in situ growth on carbon nanotubes (CNTs) followed by postsynthetic metalization with cobalt, were furnished with distinct covalent bonds (imine and quinoline, respectively) within their COF structures, conferring precise modulation of the remote microenvironment of catalytically active Co centers. Compared with its imine-linked counterpart, the quinoline-modified Co-CorCOF-3@CNT demonstrates significantly enhanced OER performance, as evidenced by a reduced overpotential, lower Tafel slope, higher current density, and increased turnover frequency. Experimental and density functional theory (DFT) calculation results jointly support the microenvironment engineering enables fine-tuning of the binding affinity of oxygen-containing intermediates to Co sites, and the change of the RDS from the formation of *OH to the deprotonation of *OH alongside a largely reduced energy barrier, thereby rationalizing the observed catalytic enhancement. This study provides critical insights into the establishment of structure–activity relationships through molecular-level manipulation of the catalytic microenvironment.

2. Results and Discussion

2.1. Design and Synthesis of Catalysts

In comparison with other extensively studied crystalline materials, such as clusters and metal–organic frameworks, COFs exhibit a simpler coordination environment and fewer factors influencing their activity, making them a more straightforward platform for investigating structure–performance relationships.[45] Building on this foundation, we designed a linear corrole unit (in contrast to our previous C_{2v}-symmetric tridentate report), for the construction of a high-symmetry model COF, which further simplifies the coordination environment. Taking advantage of the highly modifiable nature of COFs, we implemented the linkage functionalization strategy to modulate the remote microenvironment of active sites within metallocorrole-based COFs.[46] This approach circumvents the need for direct modification of building blocks, which typically requires laborious synthetic procedures.

As shown in **Figure 1a**, the parent material CorCOF-2 was synthesized through an acid-catalyzed imine condensation reaction between 10-(pentafluorophenyl)-5,15-bis(4-aminophenyl)corrole (H_3PFAC) (Figures S1–S3 and Table S1, Supporting Information) and 1,3,5-triformylbenzene (TFB) in a mixture of *n*-butanol, *o*-dichlorobenzene, and 6 M acetic acid (volume ratio of 5:5:1) at

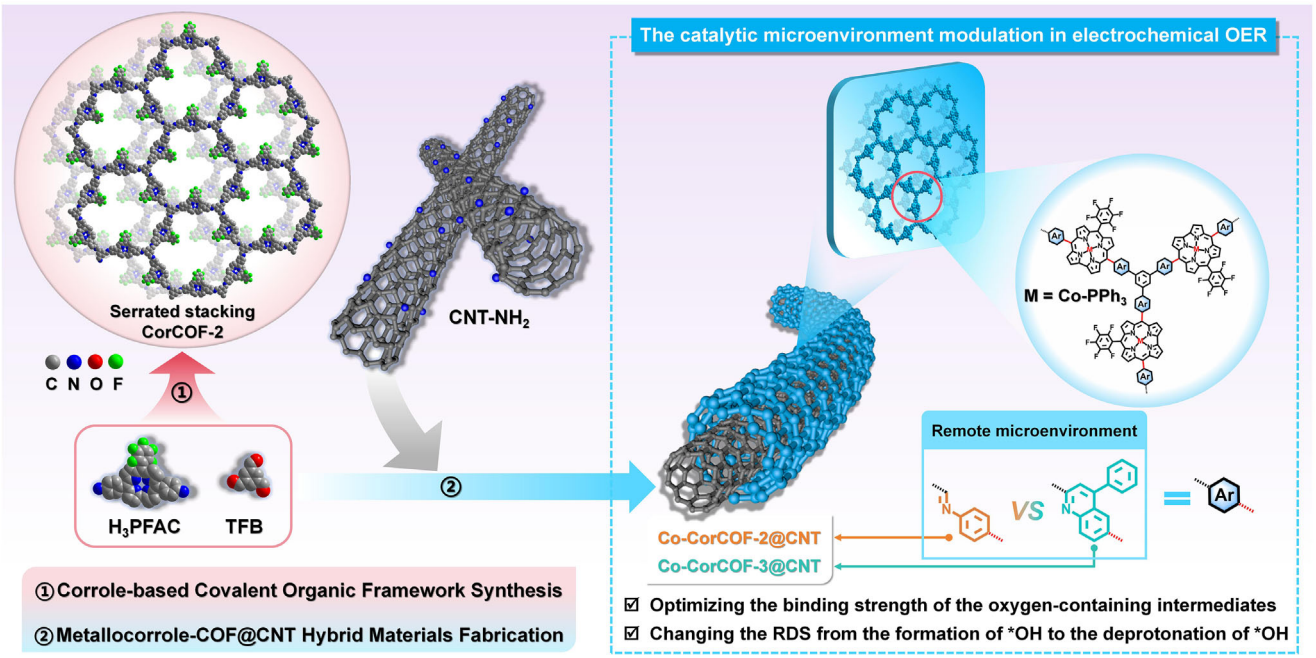

Scheme 1. Schematic illustration showing the construction of the model corrole-based COF (CorCOF-2) and Co-CorCOF@CNT hybrid materials with modulated chemical microenvironment for electrocatalytic OER.

90 °C for 72 h. Subsequently, while maintaining identical reaction conditions, the covalently hybrid material CorCOF-2@CNT was prepared in situ by introducing homogeneously dispersed amino-functionalized CNTs (CNT-NH_2). This was followed by postmetalization with Co to yield the core–shell structured Co-CorCOF-2@CNT catalyst, where CNTs serve as the core and Co-CorCOF-2 forms the shell (**Figure 2a**). To construct Co-CorCOF-3@CNT, a one-pot Povarov cycloaddition reaction was employed in conjunction with the Co-metalization process.[47] This approach enabled the functionalization of imine bonds to form quinoline linkages, providing a basis for investigating the effects of microenvironment modulation. Notably, the incorporation of CNTs as the core enhances charge transport between the current collector and the active Co-CorCOF shells during the electrocatalytic OER.

2.2. Characterization of CorCOF-2 and -3

The crystalline structure of CorCOF-2 was confirmed by the powder X-ray diffraction (PXRD) analysis in combination with in-depth theoretical simulations and N_2 sorption measurements. According to reticular chemistry, CorCOF-2 adopts an *hcb* network topology (Figure 1b). As displayed in Figure 1c, the PXRD pattern of CorCOF-2 exhibits prominent peaks, indicative of its highly crystalline nature. Given the electron-rich π surfaces and the presence of three pores along the *c*-axis within the 2D COF framework as evidenced by its porous characteristics (Figure 1h), a structural model based on a serrated stacking mode (interpreted as slipped-AA stacking) in the *P1* space group was constructed using the Materials Studio software.[48–50] In this model, adjacent sheets are offset by 1/4 of the unit cell distance (Figure 1d). The simulated PXRD pattern aligns well with the experimental data, with peaks at 2.45°, 4.71°, 6.32°, 7.14°, and 21.6° corresponding to the (110), (200), (220), (310), and (001) facets, respectively. Pawley refinements yield the unit cell parameters (a = 7.78 Å, b = 41.39 Å, c = 43.61 Å) and reliability factors, including an unweighted-profile R factor (R_p) of 2.16% and a weighted-profile R factor (R_{wp}) of 2.68%. These findings, in combination with the negligible difference plot (Figure 1c), collectively validate the proposed serrated stacking structure of CorCOF-2. Alternative structural models were also explored (Figure S4, Supporting Information), including an eclipsed arrangement in the *P3* space group (no. 143) (Figure 1e) and a staggered arrangement in the *P1* space group (Figure 1f). While the eclipsed structure's simulated PXRD pattern is in reasonable agreement with experimental data, its pore size distribution shows less consistency (Figure 1h), where a single, larger pore size of 3.1 nm is excepted. In contrast, the staggered structure's simulated pattern deviates significantly from the experimental result (Figure 1c). Besides, we investigated two additional uncommon stacking configurations (namely, inclined and antiparallel ones) to strengthen the modular arrangement of CorCOF-2.[51–53] Both simulated PXRD patterns and pore size distribution analyses conclusively demonstrate that these stacking modes are inconsistent with the experimentally determined crystal structure (Figures S5 and S6, Supporting Information). Furthermore, DFT calculations of the relative stacking energies reveal that the serrated configuration is energetically preferred (Figure S7, Supporting Information), consistent with our experimental observations.[52] Note that the serrated stacking structure is advantageous for catalysis, as it enhances the exposure of active sites to substrates and facilitates mass transfer.

The porosity and specific surface area of CorCOF-2 were evaluated using N_2 adsorption–desorption isotherms at 77 K, which

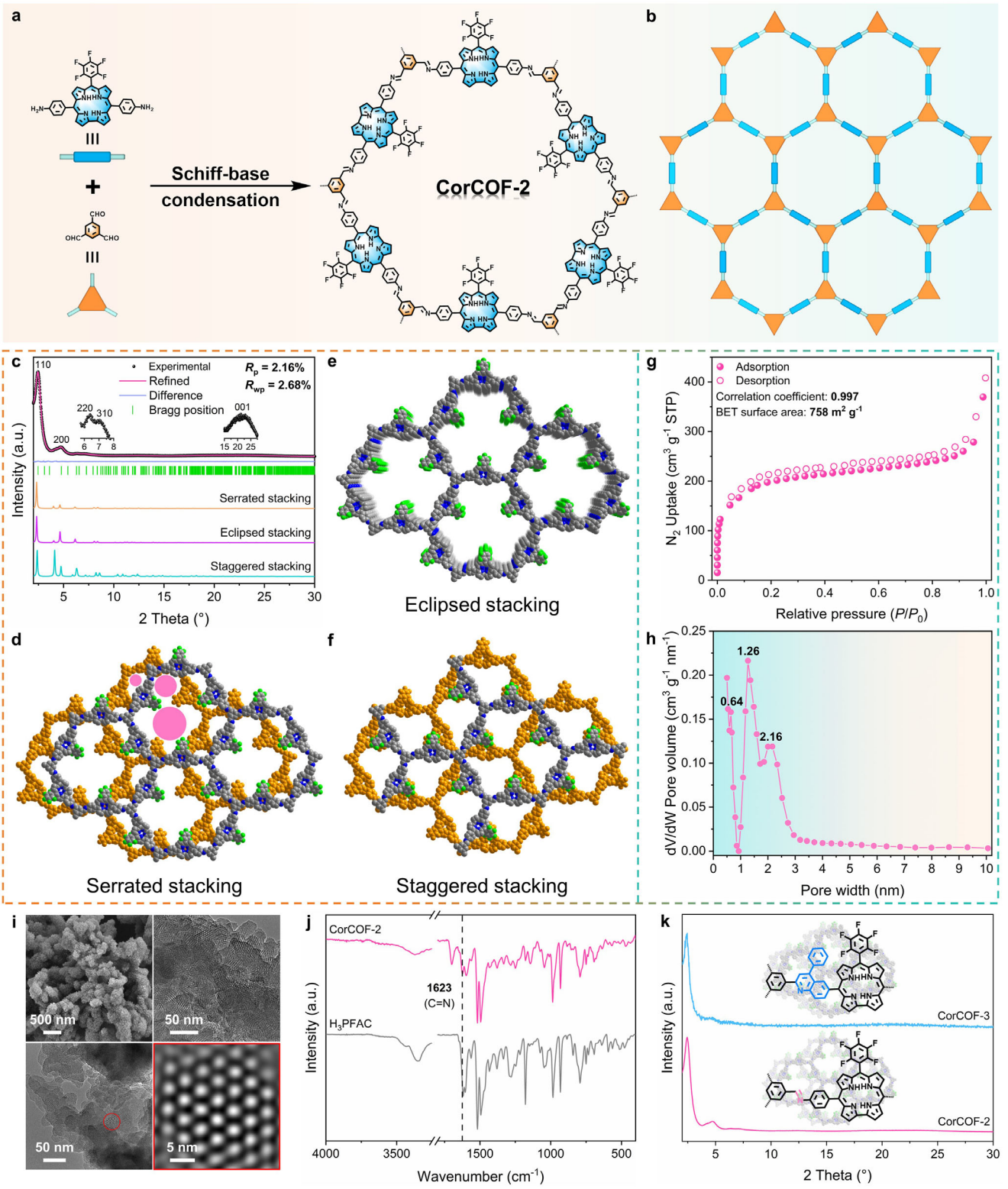

Figure 1. a) Synthetic route and b) topological net of CorCOF-2. c) PXRD characterizations for CorCOF-2 including the experimentally observed curve, Pawley refined profile and their difference, and simulated ones using the serrated, eclipsed, and staggered stacking modes. Theoretically modeled d) serrated, e) eclipsed, and f) staggered stacking structures (gray, C; blue, N; green, F; for clear clarity the H atoms were omitted). g) N_2 sorption isotherms, h) pore size distribution profile, and i) SEM and TEM images of CorCOF-2. j) FTIR spectra of CorCOF-2 and monomeric H_3PFAC. k) PXRD pattern comparison of CorCOF-3 and CorCOF-2. (Insets show the simulated structures and molecular segments.).

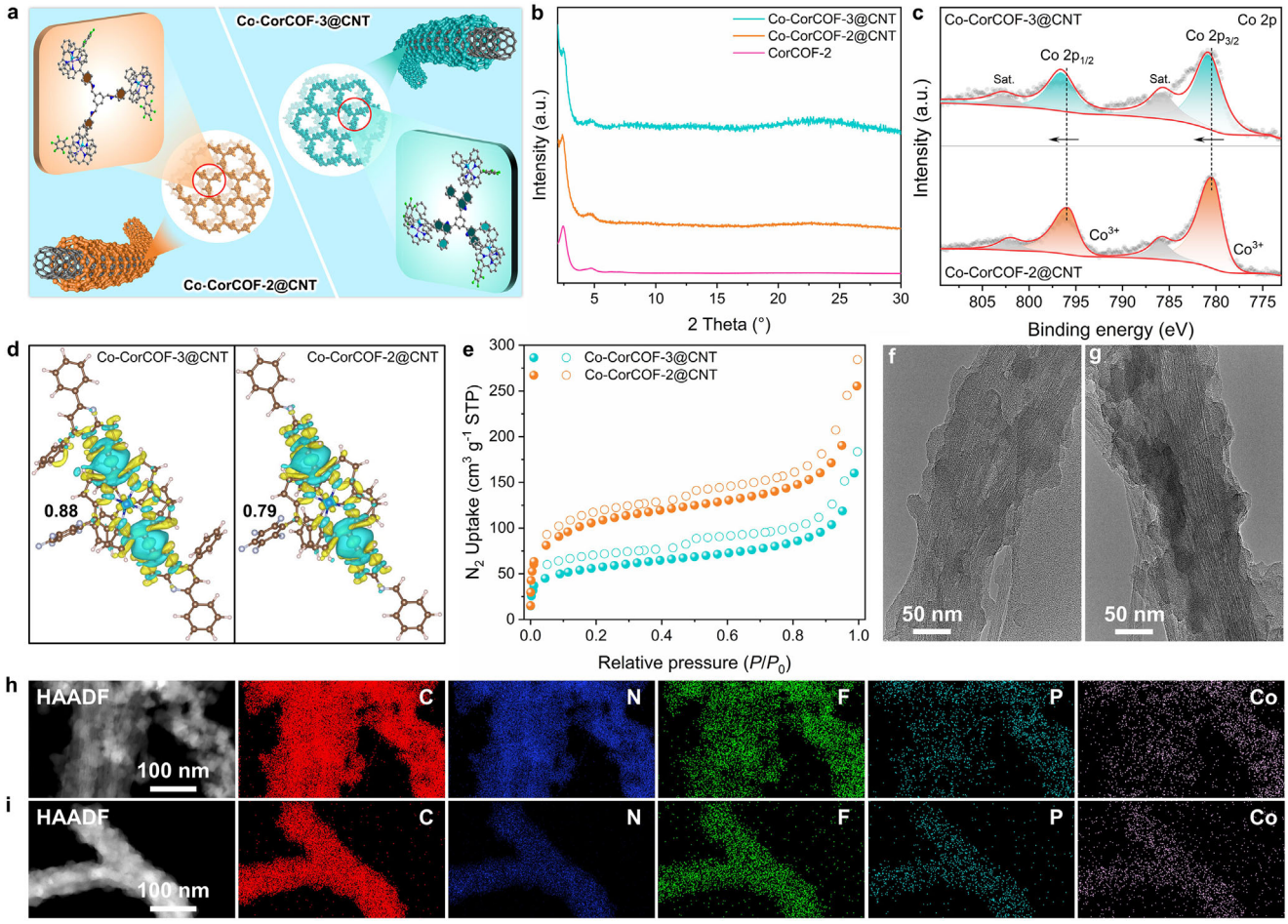

Figure 2. a) Schematic illustration of the hybrid materials of Co-CorCOF-3@CNT and Co-CorCOF-2@CNT. b) PXRD patterns of Co-CorCOF-3@CNT, Co-CorCOF-2@CNT, and CorCOF-2. c) High-resolution Co 2p XPS spectra, d) charge density difference diagram, and Bader charge, yellow and blue contours representing electron accumulation and depletion, respectively, and e) N_2 sorption isotherms of Co-CorCOF-3@CNT and Co-CorCOF-2@CNT. TEM images and EDS elemental mappings of f,h) Co-CorCOF-3@CNT and g,i) Co-CorCOF-2@CNT, respectively.

exhibit a characteristic type-I sorption curve (Figure 1g,h). The Brunauer–Emmett–Teller (BET) surface area was calculated to be 758 $m^2\ g^{-1}$ on the basis of the N_2 adsorption data. Nonlocal density functional theory analysis of the pore size distribution indicates the coexistence of micropores and mesopores, with predominant pore sizes at 0.64, 1.26, and 2.16 nm, consistent with the simulated values from the serrated stacking model. As shown in Figure 1i, the scanning electron microscopy (SEM) image of CorCOF-2 indicates a sphere-like morphology composed of aggregated granular crystallites. High-resolution transmission electron microscopy images reveal distinct lattice fringes and well-defined hexagonal lattices, further confirming the long-range ordered structure, which is consistent with the PXRD results. Besides, the chemical structure of CorCOF-2 was verified using Fourier-transform infrared (FTIR) spectroscopy and ^{13}C solid-state cross-polarization magic-angle-spinning (CP/MAS) NMR spectroscopy. The FTIR spectrum shows a typical imine stretching vibration band at 1623 cm^{-1} (Figure 1j), while the ^{13}C CP/MAS NMR spectrum exhibits a resonance signal for the imine carbon (C═N) at 158.6 ppm (Figure S8, Supporting Information), collectively manifesting the successful synthesis of imine-linked CorCOF-2. Furthermore, the structure of CorCOF-3, which features quinoline linkages, was thoroughly characterized using analogous techniques (Figure 1k; Figures S9,S10, and S14, Supporting Information). The results demonstrate the formation of quinoline bonds through imine functionalization, as well as the material's high crystallinity, large surface area, and isostructural similarity to CorCOF-2. Notably, the structural variation in CorCOFs, while preserving the identical framework, offers an ideal model platform for exploring the effects of microenvironmental factors.

2.3. Characterization of Co-CorCOF@CNT Hybrids

Following covalent polymerization in the presence of CNTs and subsequent postmetalization, the ordered crystalline structures of the resulting Co-CorCOF-2@CNT and Co-CorCOF-3@CNT are maintained. This preservation is evidenced by the similarity in PXRD patterns between the synthesized materials and the parent COF (Figure 2b). FTIR spectra reveal new stretching vibration peaks at 520 cm^{-1} in the spectra of both hybrid materials, which

are attributed to Co–N coordination. This finding corresponds to the presence of N-coordinated Co species in Co-CorCOF@CNTs (Figure S12, Supporting Information). Further confirmation is provided by the noticeable redshifts in the corrole N signals observed in high-resolution N 1s X-ray photoelectron spectroscopy (XPS) spectra (Figure S14, Supporting Information), when compared to their metal-free counterparts. In comparison with Co-CorCOF-3, the Co 2p and P 2p spectra of Co-CorCOF-3@CNT exhibit shifts toward higher binding energies (Figures S15 and S16, Supporting Information), likely due to covalent interactions between the Co-CorCOFs and CNTs. These results collectively demonstrate the successful formation of the metalized hybrid materials. Notably, the binding energies of Co $2p_{1/2}$ and Co $2p_{2/3}$ in Co-CorCOF-3@CNT shift distinctly to 780.90 and 796.63 eV, respectively, compared to 780.46 and 796.03 eV in Co-CorCOF-2@CNT (Figure 2c). This phenomenon underscores the significant impact of microenvironment modulation, achieved through linkage functionalization, on the chemical state of isolated single Co sites. Moreover, the Co 2p XPS spectra indicate a +3 valence state for Co, which aligns with the coordination environment of the three-proton-incorporated corrole framework and is further supported by previous literature.[44,54] DFT calculations offer deeper insights into the electronic structures of Co-CorCOF@CNTs. As revealed by the charge density difference analyses and Bader charge results (Figure 2d), the Co sites in both materials undergo charge depletion, exhibiting a positive valence state. Notably, Co-CorCOF-3@CNT demonstrates a more pronounced charge loss at the Co center compared to Co-CorCOF-2@CNT, which is attributed to its enhanced π-conjugation system. This higher electron deficiency likely facilitates the adsorption and activation of negatively charged substrates, highlighting the significance of electronic modulation. Overall, the introduction of quinoline bonds in Co-CorCOF-3@CNT disrupts the electronic equilibrium between the COF backbone and the Co metal center, where the electronic redistribution may enhance the catalytic performance of Co-CorCOF-3@CNT.

N_2 sorption measurements reveal that Co-CorCOF-2@CNT and Co-CorCOF-3@CNT retain high BET surface areas of 374 and 205 $m^2\ g^{-1}$, respectively (Figure 2e). The reduced surface areas compared to the parent COFs are attributed to the incorporation of CNTs. SEM and TEM images demonstrate that both Co-CorCOF-2@CNT and Co-CorCOF-3@CNT are uniformly wrapped onto CNTs, in stark contrast with the smooth surface of pristine CNTs (Figures S18 and S19, Supporting Information; Figure 2f,g). High-angle annular dark-field scanning TEM images and corresponding energy-dispersive X-ray spectroscopy (EDS) mappings confirm the homogeneous distribution of C, N, F, P, and Co elements throughout the Co-CorCOF@CNT architectures (Figure 2h,i), consistent with XPS analyses (Figure S13, Supporting Information). Inductively coupled plasma mass spectrometry measurements determine the Co content in Co-CorCOF-2@CNT and Co-CorCOF-3@CNT to be 2.7 and 2.4 wt%, respectively.

To better elucidate the chemical state, dispersion, and local coordination environment of Co species in the hybrid materials, X-ray absorption near-edge structure (XANES) and Fourier-transform extended X-ray absorption fine structure (FT-EXAFS) measurements were performed. For this study, Co-CorCOF-3@CNT was selected as a representative sample, with commercial Co foil, CoO, and Co_2O_3 serving as benchmarks for comparison. As shown in **Figure 3a**, the XANES spectrum of Co-CorCOF-3@CNT exhibits a distinct profile compared to the reference samples, reflecting their intrinsically different coordination environments. The normalized Co K-edge absorption threshold of Co-CorCOF-3@CNT closely aligns with that of Co_2O_3, suggesting a +3 oxidation state for Co, which is in agreement with the XPS results. Furthermore, the FT-EXAFS spectrum of Co-CorCOF-3@CNT displays a dominant peak at ≈1.6 Å, attributable to Co–N coordination in the first-shell region (Figure 3b), while the absence of a Co–Co peak (≈2.11 Å) confirms the atomic dispersion of Co sites within the catalyst. To further validate this finding, wavelet transform EXAFS (WT-EXAFS) analysis reveals a single intensity maximum at 4.5 $Å^{-1}$ corresponding to Co–N, which is clearly distinguished from Co–Co and Co–O scattering paths, ruling out the presence of Co-based metallic or oxide nanoparticles (Figure 3d). Quantitative EXAFS fitting analysis indicates that the isolated Co atoms in Co-CorCOF-3@CNT are coordinated with four N atoms in the first shell as the Co–N_4 configuration (Figure 3c; Table S2, Supporting Information), consistent with our synthetic design. The presence of such well-defined, uniform single Co sites provides an ideal platform for investigating microenvironment regulation mechanisms.

2.4. OER Activity Evaluation

The successful fabrication of structurally diverse Co-CorCOF@CNT electrocatalysts with precisely defined chemical environments provides a valuable platform for probing into structure–activity relationships through microenvironment modulation. We evaluated the electrochemical OER performance of Co-CorCOF@CNTs using linear sweep voltammetry (LSV) in a standard three-electrode system with 1.0 M KOH electrolyte. For comparison, monomeric Co-Cor, CNT-NH_2, pristine Co-CorCOF-3, and commercial RuO_2 were also tested. The working electrode was prepared by drop-casting catalyst ink onto carbon paper with an optimized mass loading of 0.3 mg cm^{-2} (Figure S21, Supporting Information). As displayed in **Figure 4a**, the LSV polarization curves demonstrate that Co-CorCOF-3@CNT exhibits superior catalytic activity, requiring an overpotential of only 357 mV to achieve a current density of 10 mA cm^{-2}. This performance surpasses that of Co-CorCOF-2@CNT (387 mV), Co-CorCOF-3 (448 mV), and Co-Cor (480 mV), while the conductive CNT-NH_2 substrate exhibits negligible activity, highlighting the catalytic role of Co-CorCOFs (Figure S22, Supporting Information). Although Co-CorCOF-3@CNT shows a slightly higher overpotential than RuO_2 at 10 mA cm^{-2}, it outperforms RuO_2 at higher current densities, requiring only 408 mV at 50 mA cm^{-2} compared to 492 mV for RuO_2 (Figure 4b). Notably, Co-CorCOF-3@CNT achieves a maximum current density of 668 mA cm^{-2}, corresponding to a mass activity of 2226.7 A g^{-1}, which represents a 1.65-fold increase over Co-CorCOF-2@CNT (404 mA cm^{-2}) and exceeds the performance of other reported COF-based catalysts (Figure 4c,d; Table S3, Supporting Information). Tafel analysis, derived from the LSV curves, provides insights into the OER electrocatalytic kinetics. Co-CorCOF-3@CNT exhibits

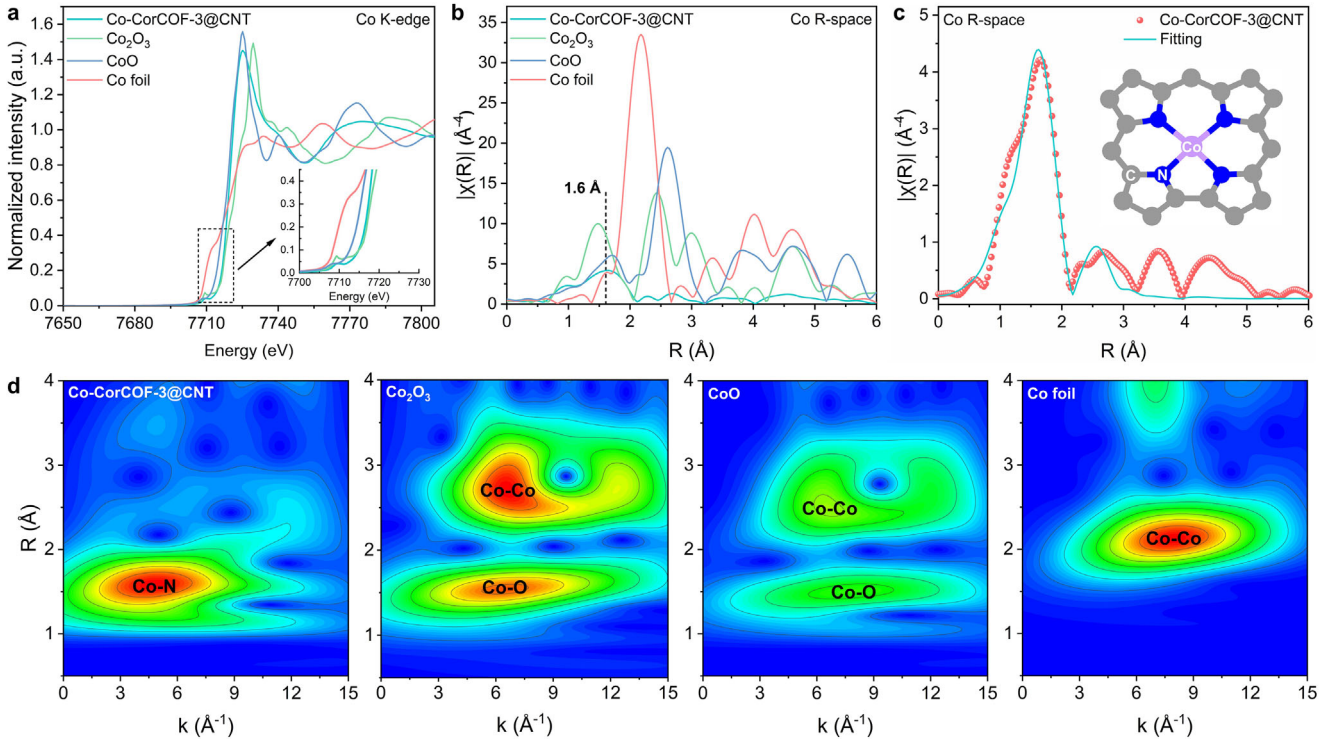

Figure 3. a) Co K-edge XANES and b) FT-EXAFS spectra of Co-CorCOF-3@CNT, Co_2O_3, CoO, and Co foil. c) EXAFS fitting of Co-CorCOF-3@CNT in *R* space. (The inset shows the corresponding structure.) d) WT-EXAFS plots of Co-CorCOF-3@CNT, Co_2O_3, CoO, and Co foil, respectively.

the lowest Tafel slope of 62 mV dec^{-1} (Figure 4e), indicating exceptional catalytic kinetics. These results highlight that Co-CorCOF-3@CNT performs comparably to commercial RuO_2, underscoring its potential for electrocatalytic water oxidation. Furthermore, the enhanced activity of Co-CorCOF-3 over Co-Cor emphasizes the importance of heterogenizing molecular catalysts. The improved performance of Co-CorCOF-3@CNT relative to pristine Co-CorCOF-3 can be attributed to the incorporation of conductive substrates, which facilitate electron transfer. More importantly, the comparative results for both Co-CorCOF@CNTs unequivocally indicate that precise control over the chemical microenvironment significantly enhances electrochemical performance.

To further elucidate the microenvironment effects, the electrochemical surface area of Co-CorCOF-2@CNT and Co-CorCOF-3@CNT was evaluated by calculating the double-layer capacitance (C_{dl}) (Figure S23, Supporting Information). The C_{dl} values for Co-CorCOF-2@CNT and Co-CorCOF-3@CNT are 2.4 and 3.1 mF cm^{-2}, respectively (Figure 4f), indicating similar densities of exposed active sites. This suggests that the observed differences in catalytic performance are not due to variations in active site availability. Turnover frequency (TOF) calculations based on Co site loading further reveal that Co-CorCOF-3@CNT exhibits higher TOF values across the tested potential range, reaching 8.2 s^{-1} at an overpotential of 520 mV, compared to 4.0 s^{-1} for Co-CorCOF-2@CNT (Figure 4g). This significant difference in TOF underscores the superior catalytic activity of Co-CorCOF-3@CNT. Additionally, water-vapor sorption curves (Figure 4h) indicate comparable hydrophilicity for both materials, ruling out surface wettability as a contributing factor to the enhanced performance of Co-CorCOF-3@CNT. Overall, these results manifest that microenvironment modulation enhances the intrinsic activity of single Co sites, leading to higher TOF and improved catalytic efficiency despite similar active site densities and hydrophilic properties.

Electrochemical impedance spectroscopy (EIS) was employed to investigate the electronic transport capabilities of Co-CorCOF-2@CNT and Co-CorCOF-3@CNT (Figure 4i). The Nyquist plots show that Co-CorCOF-3@CNT exhibits significantly lower charge transfer resistance (R_{ct}) than Co-CorCOF-2@CNT, consistent with its faster electron transfer kinetics as inferred from Tafel analysis. This further corroborates the superior OER performance of Co-CorCOF-3@CNT. Both materials exhibit Faradaic efficiencies exceeding 98%, indicating high selectivity for the oxygen evolution process (Figure S24, Supporting Information). The stabilities of Co-CorCOF-3@CNT and Co-CorCOF-2@CNT were also examined. Long-term chronopotentiometric testing at a constant current density of 10 mA cm^{-2} over 18 h further confirms the Co-CorCOF-3@CNT's durability (Figure S25, Supporting Information), while Co-CorCOF-2@CNT undergoes severe OER performance decay. Specifically, for Co-CorCOF-3@CNT, after 1000 cyclicvoltammetry cycles, the overpotential at 10 mA cm^{-2} increases by less than 10 mV (Figure S26, Supporting Information). Postcatalytic characterizations, including XRD, FTIR, XPS, XANES, FT-EXAFS, and SEM indicate that the crystallinity, chemical structure, and morphology of Co-CorCOF-3@CNT remain intact after OER cycling (Figure S27). These results collectively demonstrate the robust catalytic stability of Co-CorCOF-3@CNT under electrochemical conditions.

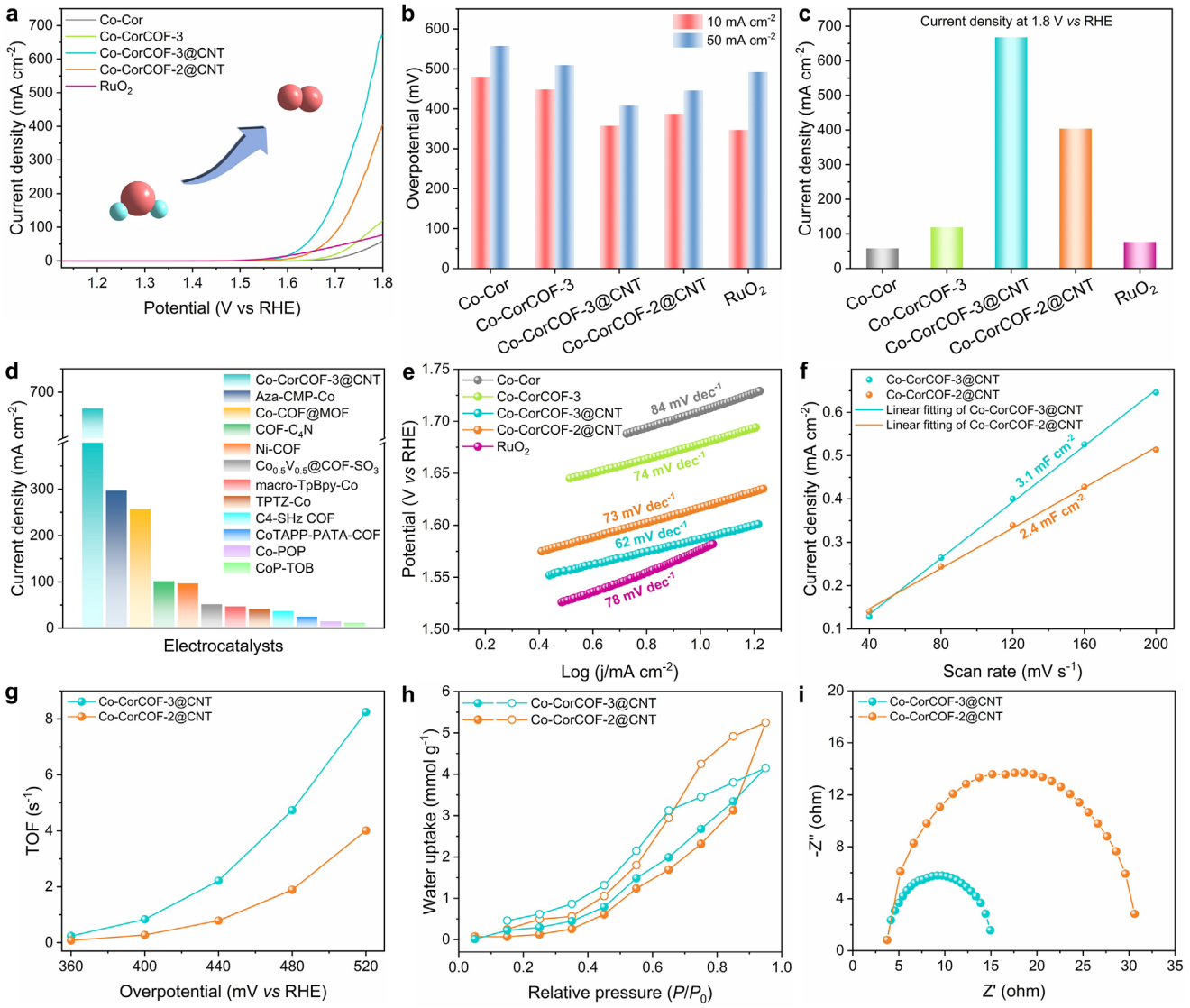

Figure 4. a) LSV polarization curves, b) overpotentials at 10 and 50 mA cm^{-2}, c) current densities at 1.8 V versus RHE, and e) Tafel plots of Co-Cor, Co-CorCOF-3, Co-CorCOF-3@CNT, Co-CorCOF-2@CNT, and RuO_2. d) Comparison of current density for Co-CorCOF-3@CNT with the reported representative COF-based OER electrocatalysts (see refs. S14–S24 in Supporting Information). f) The C_{dl} values, g) TOFs versus various overpotentials, h) water-vapor sorption curves, and i) EIS Nyquist plots of Co-CorCOF-3@CNT and Co-CorCOF-2@CNT.

2.5. Electrocatalytic Mechanism

To gain a comprehensive understanding of the microenvironment modulation effect in Co-CorCOF@CNTs, we conducted DFT calculations to investigate the electronic properties and the electrocatalytic OER mechanism. Given the significant influence of linkage functionalization on the OER activity of Co-CorCOF@CNTs, we constructed two theoretical models, Co-Cor-2 and Co-Cor-3, featuring distinct linkages, to analyze their electrocatalytic processes (**Figure** 5a; Figure S28, Supporting Information). The adsorption of three OER intermediates (*OH, *O, and *OOH) on the Co sites was optimized to determine the corresponding Gibbs free energy values at $U = 0$ V. A comparative analysis of the OER processes for Co-Cor-2 and Co-Cor-3 (Figure 5b) reveals that the RDS for Co-Cor-3 occurs during the transition from *OH to *O, with a theoretical overpotential of 0.37 V and a corresponding free energy change (ΔG) of 1.60 eV. This overpotential is notably lower than that of Co-Cor-2 (0.50 V), indicating that the linkage functionalization in Co-CorCOF-3@CNT activates the isolated single Co site and regulates its binding strength of OER intermediates.[52] This optimization generates more efficient catalytic active sites, thereby enhancing the overall catalytic performance, which aligns well with our experimental observations (Figure 4a,b).

Furthermore, we analyzed the projected density of states (PDOS) of the Co-d orbitals for Co-CorCOF-2 and Co-CorCOF-3 (Figure 5c; Figure S29, Supporting Information). The d-band center of the Co atom in Co-CorCOF-3 (−1.145 eV) is shifted closer to the Fermi level compared to that of Co-CorCOF-2 (−1.896 eV). This shift positively influences the catalytic

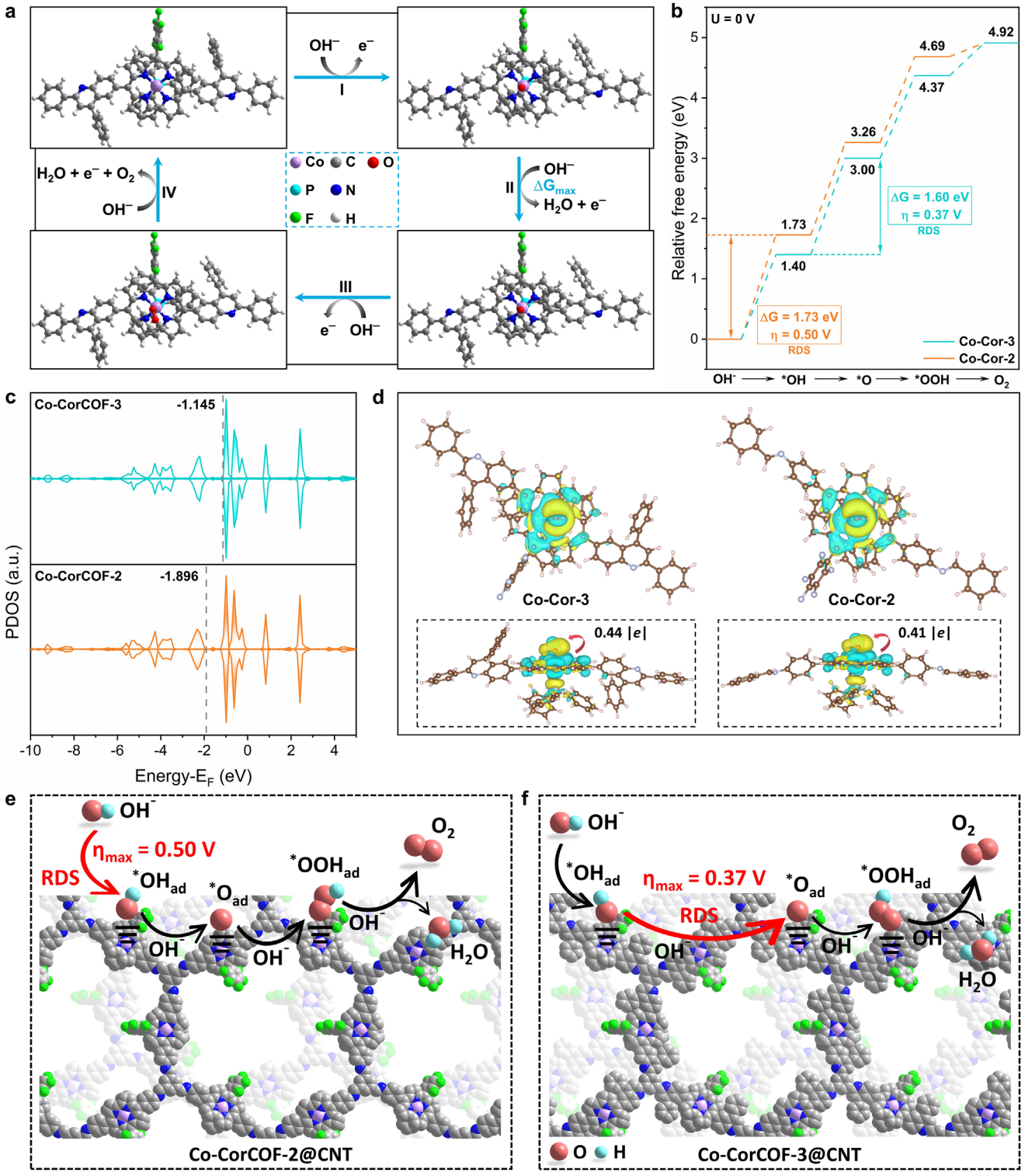

Figure 5. a) Proposed catalytic OER mechanism of the Co-CorCOF-3@CNT model. b) Gibbs free energy diagrams of the Co-CorCOF-3@CNT and Co-CorCOF-2@CNT models for OER reaction at $U = 0$ V. c) PDOS of single Co active sites in Co-CorCOF-3 and Co-CorCOF-2; the d-band centers are labeled. d) Charge density difference and Bader charge analysis of the catalyst models with the intermediate *OH. Schematic illustration of the OER reaction processes for e) Co-CorCOF-2@CNT and f) Co-CorCOF-3@CNT.

process by strengthening the adsorption of oxygenated intermediates, thereby accelerating reaction kinetics and improving electrocatalytic efficiency.[55,56] Additionally, charge density difference and Bader charge calculations were performed to investigate the interaction between the catalysts and the key intermediate *OH (Figure 5d). The results demonstrate that Co-Cor-3 transfers more charge to *OH than Co-Cor-2, indicating a stronger binding strength between Co-Cor-3 and *OH, which contributes to the enhancement of OER activity.[54]

Overall, modulating the remote microenvironment of single Co active sites enhances the adsorption of reaction substrates and oxygen-containing intermediates, leading to improved catalytic activity for OER. Compared to Co-CorCOF-2@CNT, the quinoline-functionalized Co-CorCOF-3@CNT effectively regulates the free energy of reaction intermediates, resulting in a lower OER overpotential and superior catalytic performance. This confirms that the Co-CorCOF-3@CNT structure is more favorable for electrocatalytic OER. As illustrated in the schematic diagrams of the OER reaction processes for Co-CorCOF-2@CNT and Co-CorCOF-3@CNT (Figure 5e,f), Co-CorCOF-3@CNT modifies the RDS of the OER from the *OH formation to the *OH deprotonation, accompanied by a significant reduction in the energy barrier. This microenvironment modulation strategy presents a promising approach for optimizing electrocatalytic processes.

3. Conclusion

In summary, this work clearly demonstrates the tunability of OER activity and electrocatalytic behavior by tailoring the remote microenvironment of catalytic centers through functionalizing COF linkages. To achieve this, we developed and modeled covalently integrated structures with well-defined Co-CorCOFs as the shell and carbon nanotubes as the core, and these hybrids feature highly accessible single Co sites and favorable conductivity. Notably, quinoline modifications to the COF linkage disrupt the electronic equilibrium between the COF backbone and the active Co centers in Co-CorCOF-3@CNT, optimizing the intrinsic activity of Co sites. It, therefore, leads to a substantial promotion in the electrocatalytic performance toward OER, as evidenced by a low overpotential (357 mV at 10 mA cm^{-2}), a small Tafel slope (62 mV dec^{-1}), and high current density (668 mA cm^{-2}) and TOF (8.2 s^{-1}), outperforming Co-CorCOF-2@CNT. DFT calculations have revealed that precise modulation of the microenvironment around active sites positively regulates the d-band center of Co atoms, optimizes the binding energy between the Co sites and reaction intermediates, and modifies the RDS of the reaction kinetics, thereby enhancing OER performance. This study not only represents the first exploration of metallocorrole-based COFs for electrochemical applications, but also provides a molecular-level microenvironment modulation strategy as a versatile paradigm for designing high-performance catalysts, which could be readily extended to other catalytic systems and applications.

Supporting Information

Supporting Information is available from the Wiley Online Library or from the author.

Acknowledgements

The authors acknowledge the National Natural Science Foundation of China (No. 22201258) and the China Postdoctoral Science Foundation (Nos. 2023TQ0323 and 2024M752928) for financial support of this work. Support in part from the Robert A. Welch Foundation (B-0027) (S.M.) and Princess Nourah bint Abdulrahman University Researchers Supporting Project (PNURSP2025R1), Riyadh, Saudi Arabia (T.A.) is also acknowledged.

Conflict of Interest

The authors declare no conflict of interest.

Data Availability Statement

The data that support the findings of this study are available from the corresponding author upon reasonable request.

Keywords

corrole, covalent organic frameworks, electrocatalysis, microenvironment modulation, oxygen evolution reaction

Received: May 13, 2025
Revised: July 17, 2025
Published online:

[1] B. Zhang, X. Zheng, O. Voznyy, R. Comin, M. Bajdich, M. García-Melchor, L. Han, J. Xu, M. Liu, L. Zheng, F. P. García de Arquer, C. T. Dinh, F. Fan, M. Yuan, E. Yassitepe, N. Chen, T. Regier, P. Liu, Y. Li, P. De Luna, A. Janmohamed, H. L. Xin, H. Yang, A. Vojvodic, E. H. Sargent, *Science* **2016**, *352*, 333.
[2] S. Chu, A. Majumdar, *Nature* **2012**, *488*, 294.
[3] R. H. Coridan, A. C. Nielander, S. A. Francis, M. T. McDowell, V. Dix, S. M. Chatman, N. S. Lewis, *Energy Environ. Sci.* **2015**, *8*, 2886.
[4] S. Li, B. Chen, Y. Wang, M.-Y. Ye, P. A. van Aken, C. Cheng, A. Thomas, *Nat. Mater.* **2021**, *20*, 1240.
[5] J. Zhao, Y. Guo, Z. Zhang, X. Zhang, Q. Ji, H. Zhang, Z. Song, D. Liu, J. Zeng, C. Chuang, E. Zhang, Y. Wang, G. Hu, M. A. Mushtaq, W. Raza, X. Cai, F. Ciucci, *Nat. Nanotechnol.* **2025**, *20*, 57.
[6] R. Matheu, P. Garrido-Barros, M. Gil-Sepulcre, M. Z. Ertem, X. Sala, C. Gimbert-Suriñach, A. Llobet, *Nat. Rev. Chem.* **2019**, *3*, 331.
[7] H. Yang, F. Li, S. Zhan, Y. Liu, W. Li, Q. Meng, A. Kravchenko, T. Liu, Y. Yang, Y. Fang, L. Wang, J. Guan, I. Furó, M. S. G. Ahlquist, L. Sun, *Nat. Catal.* **2022**, *5*, 414.
[8] D.-G. Wang, T. Qiu, W. Guo, Z. Liang, H. Tabassum, D. Xia, R. Zou, *Energy Environ. Sci.* **2021**, *14*, 688.
[9] C. H. Sharp, B. C. Bukowski, H. Li, E. M. Johnson, S. Ilic, A. J. Morris, D. Gersappe, R. Q. Snurr, J. R. Morris, *Chem. Soc. Rev.* **2021**, *50*, 11530.
[10] B. Huang, L. Li, X. Tang, W. Zhai, Y. Hong, T. Hu, K. Yuan, Y. Chen, *Energy Environ. Sci.* **2021**, *14*, 2789.
[11] R. Liu, K. T. Tan, Y. Gong, Y. Chen, Z. Li, S. Xie, T. He, Z. Lu, H. Yang, D. Jiang, *Chem. Soc. Rev.* **2021**, *50*, 120.
[12] A. Rodríguez-Camargo, K. Endo, B. V. Lotsch, *Angew. Chem., Int. Ed.* **2024**, *63*, 202413096.
[13] X. Zhao, P. Pachfule, A. Thomas, *Chem. Soc. Rev.* **2021**, *50*, 6871.
[14] N. A. Rejali, M. Dinari, Y. Wang, *Chem. Commun.* **2023**, *59*, 11631.
[15] Q. Guan, L.-L. Zhou, Y.-B. Dong, *J. Am. Chem. Soc.* **2023**, *145*, 1475.

[16] X. Li, S. Cai, B. Sun, C. Yang, J. Zhang, Y. Liu, *Matter* **2020**, *3*, 1507.
[17] R. P. Bisbey, W. R. Dichtel, *ACS Cent. Sci.* **2017**, *3*, 533.
[18] H. Duan, K. Li, M. Xie, J.-M. Chen, H.-G. Zhou, X. Wu, G.-H. Ning, A. I. Cooper, D. Li, *J. Am. Chem. Soc.* **2021**, *143*, 19446.
[19] X. Guan, F. Chen, S. Qiu, Q. Fang, *Angew. Chem., Int. Ed.* **2023**, *62*, 202213203.
[20] J. Wang, N. Li, Y. Xu, H. Pang, *Chem. - Eur. J.* **2020**, *26*, 6402.
[21] J. Tang, Z. Liang, H. Qin, X. Liu, B. Zhai, Z. Su, Q. Liu, H. Lei, K. Liu, C. Zhao, R. Cao, Y. Fang, *Angew. Chem., Int. Ed.* **2023**, *62*, 202214449.
[22] M. Liu, S. Liu, C.-X. Cui, Q. Miao, Y. He, X. Li, Q. Xu, G. Zeng, *Angew. Chem., Int. Ed.* **2022**, *61*, 202213522.
[23] W. Zhou, L. Yang, X. Wang, W. Zhao, J. Yang, D. Zhai, L. Sun, W. Deng, *JACS Au* **2021**, *1*, 1497.
[24] H. Jia, N. Yao, Y. Jin, L. Wu, J. Zhu, W. Luo, *Nat. Commun.* **2024**, *15*, 5419.
[25] C. Lin, H. Ma, J.-R. He, Q. Xu, M. Song, C.-X. Cui, Y. Chen, C.-X. Li, M. Jiao, L. Zhai, *Small* **2024**, *20*, 2403775.
[26] L. Jiao, J. Wang, H.-L. Jiang, *Acc. Mater. Res.* **2021**, *2*, 327.
[27] G. Yang, D. Wang, Y. Wang, W. Hu, S. Hu, J. Jiang, J. Huang, H.-L. Jiang, *J. Am. Chem. Soc.* **2024**, *146*, 10798.
[28] S. Hu, M.-L. Gao, J. Huang, H. Wang, Q. Wang, W. Yang, Z. Sun, X. Zheng, H.-L. Jiang, *J. Am. Chem. Soc.* **2024**, *146*, 20391.
[29] M. Guo, Q. Meng, W. Chen, Z. Meng, M.-L. Gao, Q. Li, X. Duan, H.-L. Jiang, *Angew. Chem., Int. Ed.* **2023**, *62*, 202305212.
[30] S. Suleman, Y. Zhang, Y. Qian, J. Zhang, Z. Lin, Ö. Metin, Z. Meng, H.-L. Jiang, *Angew. Chem., Int. Ed.* **2024**, *63*, 202314988.
[31] S. Yang, R. Sa, H. Zhong, H. Lv, D. Yuan, R. Wang, *Adv. Funct. Mater.* **2022**, *32*, 2110694.
[32] T. Xie, S. Chen, Y. Yue, T. Sheng, N. Huang, Y. Xiong, *Angew. Chem., Int. Ed.* **2024**, *63*, 202411188.
[33] Q. Chen, D.-H. Si, Q.-J. Wu, R. Cao, Y.-B. Huang, *Adv. Funct. Mater.* **2024**, *34*, 2315368.
[34] Q. Li, L. Luo, X. Guo, R. Wang, J. Liu, W. Fan, Z. Feng, F. Zhang, *J. Am. Chem. Soc.* **2025**, *147*, 1884.
[35] A. Mahammed, Z. Gross, *J. Am. Chem. Soc.* **2023**, *145*, 12429.
[36] C. Di Natale, C. P. Gros, R. Paolesse, *Chem. Soc. Rev.* **2022**, *51*, 1277.
[37] Y. Zhao, S. Qi, Z. Niu, Y. Peng, C. Shan, G. Verma, L. Wojtas, Z. Zhang, B. Zhang, Y. Feng, Y.-S. Chen, S. Ma, *J. Am. Chem. Soc.* **2019**, *141*, 14443.
[38] Y. Zhao, W. Dai, Y. Peng, Z. Niu, Q. Sun, C. Shan, H. Yang, G. Verma, L. Wojtas, D. Yuan, Z. Zhang, H. Dong, X. Zhang, B. Zhang, Y. Feng, S. Ma, *Angew. Chem., Int. Ed.* **2020**, *59*, 4354.
[39] Y. Zhao, Y. Peng, C. Shan, Z. Lu, L. Wojtas, Z. Zhang, B. Zhang, Y. Feng, S. Ma, *Nano Res.* **2022**, *15*, 1145.
[40] H. Lei, X. Li, J. Meng, H. Zheng, W. Zhang, R. Cao, *ACS Catal.* **2019**, *9*, 4320.
[41] W. Sinha, A. Mahammed, N. Fridman, Z. Gross, *ACS Catal.* **2020**, *10*, 3764.
[42] X. Li, H. Qin, J. Han, X. Jin, Y. Xu, S. Yang, W. Zhang, R. Cao, *Adv. Funct. Mater.* **2024**, *34*, 2310820.
[43] H. Lei, Q. Zhang, Z. Liang, H. Guo, Y. Wang, H. Lv, X. Li, W. Zhang, U.-P. Apfel, R. Cao, *Angew. Chem., Int. Ed.* **2022**, *61*, 202201104.
[44] A. Aljabour, H. Awada, L. Song, H. Sun, S. Offenthaler, F. Yari, M. Bechmann, M. C. Scharber, W. Schöfberger, *Angew. Chem., Int. Ed.* **2023**, *62*, 202302208.
[45] X.-Y. Dong, H. Chen, S. Wang, R.-Y. Zou, S.-Q. Zang, J. M. Cai, *Adv. Mater.* **2025**, *37*, 2413710.
[46] C. S. Diercks, S. Lin, N. Komienko, E. A. Kapustin, E. M. Nichols, C. Zhu, Y. Zhao, C. J. Chang, O. M. Yaghi, *J. Am. Chem. Soc.* **2018**, *140*, 1116.
[47] X.-T. Li, J. Zou, T.-H. Wang, H.-C. Ma, G.-J. Chen, Y.-B. Dong, *J. Am. Chem. Soc.* **2020**, *142*, 6521.
[48] Q. Fang, Z. Zhuang, S. Gu, R. B. Kaspar, J. Zheng, J. Wang, S. Qiu, Y. Yan, *Nat. Commun.* **2014**, *5*, 4503.
[49] X. Chen, Q. Dang, R. Sa, L. Li, L. Li, J. Bi, Z. Zhang, J. Long, Y. Yu, Z. Zou, *Chem. Sci.* **2020**, *11*, 6915.
[50] L. Zhang, Y. Zhou, M. Jia, Y. He, W. Hu, Q. Liu, J. Li, X. Xu, C. Wang, A. Carlsson, S. Lazar, A. Meingast, Y. Ma, J. Xu, W. Wen, Z. Liu, J. Cheng, H. Deng, *Matter* **2020**, *2*, 1049.
[51] A. M. Pütz, M. W. Terban, S. Bette, F. Haase, R. E. Dinnebier, B. V. Lotsch, *Chem. Sci.* **2020**, *11*, 12647.
[52] C. E. Pelkowski, A. Natraj, C. D. Malliakas, D. W. Burke, M. I. Bardot, Z. Wang, H. Li, W. R. Dichtel, *J. Am. Chem. Soc.* **2023**, *145*, 21798.
[53] X. Li, J. Qiao, S. W. Chee, H.-S. Xu, X. Zhao, H. S. Choi, W. Yu, S. Y. Quek, U. Mirsaidov, K. P. Loh, *J. Am. Chem. Soc.* **2020**, *142*, 4932.
[54] R. Ma, C. Tang, Y. Wang, X. Xu, M. Wu, X. Cui, Y. Yang, *Angew. Chem., Int. Ed.* **2024**, *63*, 202405594.
[55] J. Ke, W. Zhu, Y. Ji, J. Chen, C. Li, Y. Wang, Q. Wang, W.-H. Huang, Z. Hu, Y. Li, Q. Shao, J. Lu, *Angew. Chem., Int. Ed.* **2025**, *137*, 202422740.
[56] J. Zhang, H. Chen, S. Liu, L.-D. Wang, X.-F. Zhang, J.-X. Wu, L.-H. Yu, X.-H. Zhang, S. Zhong, Z.-Y. Du, C.-T. He, X.-M. Chen, *J. Am. Chem. Soc.* **2023**, *145*, 20000.